# An eddy viscosity model for two-dimensional breaking waves and its validation with laboratory experiments

Zhigang Tian,[1] Marc Perlin,[2] and Wooyoung Choi[1,3]
[1]*Division of Ocean Systems Engineering, Korea Advanced Institute of Science and Technology (KAIST), Daejeon, South Korea*
[2]*Department of Naval Architecture and Marine Engineering, University of Michigan, Ann Arbor, Michigan, USA*
[3]*Department of Mathematical Sciences, Center for Applied Mathematics and Statistics, New Jersey Institute of Technology, Newark, New Jersey, USA*

(Received 3 May 2011; accepted 24 January 2012; published online 7 March 2012)

An eddy viscosity model to describe energy dissipation in two-dimensional breaking waves in deep water is implemented in a numerical model for the evolution of nonlinear surface waves and evaluated with experimental results. In the experiments, to develop a reliable eddy viscosity model, breaking waves are generated by both energy focusing and modulated wave groups. Local wave parameters prior to and following breaking are defined and then determined. Significant correlations between the pre-breaking and post-breaking parameters are identified and adopted in the eddy viscosity model. The numerical model detects automatically wave breaking onset based on local surface slope, determines pre-breaking local wave parameters, predicts post-breaking time and length scales, and estimates eddy viscosity to dissipate energy in wave breaking events. Numerical simulations with the model are performed and compared to the experiments. It is found that the model predicts well the total energy dissipation due to breaking waves. In addition, the computed surface elevations after wave breaking agree reasonably well with the measurements for the energy focusing (plunging) wave groups. However, for breaking wave groups due to modulational instability (plunging and spilling), a relatively large discrepancy between the surface elevation predictions and the experimental measurements is observed, in particular, at the downstream wave probe locations. This is possibly due to wave reflection and three-dimensionality in the experiments. To further validate the eddy viscosity model, the evolution of highly nonlinear irregular waves is studied numerically and the numerical solutions are compared with additional independent laboratory experiments for long-crested irregular waves. It is shown that the numerical model is capable of predicting the wave evolution subsequent to wave breaking. © *2012 American Institute of Physics*. [http://dx.doi.org/10.1063/1.3687508]

## I. INTRODUCTION

Accurate prediction of the ocean surface wave field evolution is very important for ships and offshore structures operating in severe sea states where extreme events such as freak waves can occur. Recently, much progress has been made toward deterministic prediction of ocean waves using phase-resolving nonlinear wave models.

For the prediction of water waves with broadband spectra, a pseudo-spectral method using asymptotic expansion was developed by West *et al.*[1] This method when combined with fast Fourier transform[2] has been shown to be an accurate and effective tool to simulate the nonlinear evolution of non-breaking irregular waves, for example, in Goullet and Choi.[3] In the pseudo-spectral model, wave dynamics is governed by the following system of nonlinear evolution equations for the surface

 

elevation, $\zeta$, and the velocity potential, $\Phi$, on the free surface:[1,4,5]

$$\frac{\partial \zeta}{\partial t} = \sum_{n=1}^{N} Q_n\left[\zeta, \Phi\right] \text{ and } \frac{\partial \Phi}{\partial t} = \sum_{n=1}^{N} R_n\left[\zeta, \Phi\right]. \tag{1}$$

Here $Q_n$ and $R_n$ are two nonlinear operators that can be written explicitly through recursion formulae and $N$ is the order of nonlinearity at which the original infinite series on the right-hand sides are truncated.

For nonlinear irregular waves characterized by the JONSWAP spectrum of finite bandwidth, numerical results using the pseudo-spectral model compare well with laboratory experiments,[3] and the comparison improves as the order of nonlinearity increases. Unfortunately, the simulation cannot provide reliable predictions when wave breaking occurs. In the presence of wave breaking, the wave-induced flow near the ocean surface becomes turbulent and multi-phased, and no analytical description of the flow is possible. Therefore, wave breaking effects have to be modeled in an approximate way, and then incorporated into system (1) to make a reliable prediction of ocean waves.

To model the effects of wave breaking on the evolution of steep waves, the nonlinear evolution equations given by (1) are modified to

$$\frac{\partial \zeta}{\partial t} = \sum_{n=1}^{N} Q_n\left[\zeta, \Phi\right] + D_\zeta\left[\zeta, \Phi\right] \text{ and } \frac{\partial \Phi}{\partial t} = \sum_{n=1}^{N} R_n\left[\zeta, \Phi\right] + D_\Phi\left[\zeta, \Phi\right], \tag{2}$$

where $D_\zeta$ and $D_\Phi$ are energy dissipation terms due to wave breaking. In our previous study, we developed an eddy viscosity model to simulate energy dissipation in two-dimensional unsteady plunging breakers using a boundary layer approach and dimensional analysis:[6]

$$D_\zeta\left[\zeta, \Phi\right] = 2\nu_{eddy}\frac{\partial^2 \zeta}{\partial x^2} \text{ and } D_\Phi\left[\zeta, \Phi\right] = 2\nu_{eddy}\frac{\partial^2 \Phi}{\partial x^2}, \tag{3}$$

where the eddy viscosity $\nu_{eddy}$ depends on breaking strength and can be estimated through time and length scales associated with a breaking event:

$$\nu_{eddy} = \alpha\frac{H_{br}L_{br}}{T_{br}}. \tag{4}$$

Here, $T_{br}$ is defined as the time when the wave crest begins to fall to the time when the surface disturbance front is no longer obvious; $L_{br}$ is the distance from incipient breaking to where the obvious surface disturbance ends; $H_{br}$ refers to the falling crest height;[7] $\alpha$ is a proportional constant, and $\alpha = 0.02$, as determined in Tian *et al.*[6] We showed that the eddy viscosity model predicts well the energy dissipation due to wave breaking. More surprisingly, the predicted surface elevations downstream of the breaking region have excellent agreement with experimental results. The model was also applied to examine wave frequency spectrum evolution of dispersive focusing wave groups and proved to function effectively.[8] Details of the eddy viscosity model are referred to the previous study.

However, this previously developed model is impractical in numerical simulations for real wave breaking situations, as the magnitude of the eddy viscosity, the active breaking time and location have to be measured in experiments prior to the simulations. In addition, the model was developed with experiments of plunging breakers due to wave energy focusing only. Modulational instability, wind-forcing, and wave-current interactions may also introduce wave breaking, including not only plungers, but also spilling breakers. It remains unknown whether this eddy viscosity model is appropriate for these breaking waves. Therefore, this model has to be further developed for practical numerical simulation of real ocean waves.

In this study, we conduct 2D experiments of breaking waves due to both wave energy focusing and modulational instability[9] to further refine the model. Through the experiments, the post-breaking scales, i.e., $H_{br}$, $L_{br}$, and $T_{br}$, are shown to depend on local wave parameters at wave breaking onset (pre-breaking parameters). The correlations determined are adopted for eddy viscosity estimation based on the pre-breaking parameters and Eq. (4).

The remainder of the paper is organized as follows. The experiments are described in Sec. II and results are presented in Sec. III. Section IV provides the improved eddy viscosity model, numerical simulation results, their comparison with the experimental measurements, and some discussion. Section V presents a comparison of numerical solutions for long-crested irregular waves with another laboratory experiment. Finally, Sec. VI concludes our study with discussion of future work.

## II. EXPERIMENTS

### A. Facility

Experiments are performed at Korea Advanced Institute of Science and Technology (KAIST) in a two-dimensional wave tank with glass walls and removable, transparent plastic ceiling panels. The wave tank is 15 m long, 1.5 m wide, and has a water depth as used of 0.62 m. A servo-controlled piston-type wavemaker and auxiliary electronics located at one end of the tank are used to generate water waves. At the other end of the tank, a wave absorber made of loose nets and stainless steel grids helps reduce wave reflection. A movable carriage is installed on the top of the tank and provides a work platform. Figure 1 illustrates a sketch of the wave tank and the experimental setup.

### B. Breaking wave generation

In the experiments, breaking waves due to both wave energy focusing and modulational instability are generated. For the focusing wave groups, the surface elevation, $\zeta$, is described as

$$\zeta(x,t) = \sum_{n=1}^{N} a_n \cos(k_n x - \omega_n t - \phi_n). \tag{5}$$

Here, $a_n$ is the amplitude of the $n$th wave component; $k_n$ is the wavenumber; $\omega_n = 2\pi f_n$ is the angular frequency and $f$ ranges from 1.0 to 2.4 Hz (center frequency $f_c = 1.7$ Hz and frequency bandwidth $\Delta f = 1.4$ Hz); $N = 128$ is the total number of frequency components; and $\phi_n$ is the initial phase to be determined. In addition, $x$ is the horizontal distance downstream from the wavemaker with $x = 0$ being the mean position of the wavemaker; time $t$ is relative to the initial motion of the wavemaker (i.e., $t = 0$). The linear dispersion relation is used to relate $\omega_n$ and $k_n$. Wave steepness, $k_n a_n$, for each of the components is the same and can be adjusted. Key parameters of the focusing groups are given in Table I.

Details of the generation of breaking waves through the wave focusing technique can be found in, e.g., Rapp and Melville.[10] For completeness, a brief description of the initial phase determination is presented. The phase $\phi_n$ is determined so that the wave groups focus at time $t_b$ and location $x_b$, i.e., $\cos(k_n x_b - \omega_n t_b - \phi_n) = 1$. We solve for $\phi_n$ and obtain the following equation:

$$\phi_n = k_n x_b - \omega_n t_b + 2\pi m. \tag{6}$$

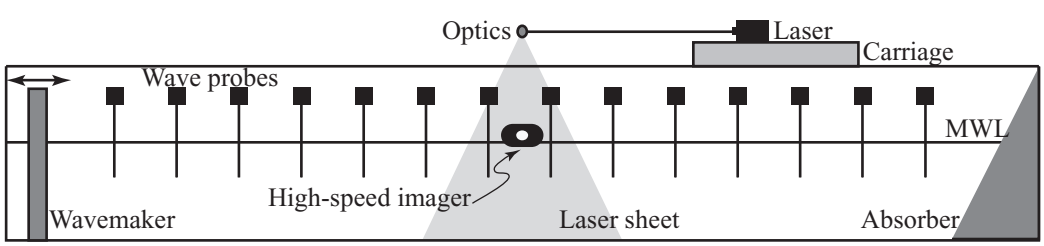


FIG. 1. Illustration of the two-dimensional wave tank (not to scale) and measurement devices.

TABLE I. Specified parameters for the energy focusing wave groups. Note that EF 1 is a non-breaking wave group while the remainder are breaking groups.

| Wave group | $f_c$ (Hz) | $\Delta f/f_c$ | $\varepsilon_n = k_n a_n$ |
|---|---|---|---|
| EF 1 | 1.7 | 0.824 | 0.0020 |
| EF 2 | 1.7 | 0.824 | 0.0032 |
| EF 3 | 1.7 | 0.824 | 0.0045 |
| EF 4 | 1.7 | 0.824 | 0.0058 |

Here, m = 0, ±1, ±2, . . . Then, by substituting (6) into (5) and setting $x = 0$, the surface elevation at the wave-maker can be obtained as

$$\zeta(0, t) = \sum_{n=1}^{N} a_n \cos\left[-k_n x_b - \omega_n (t - t_b)\right]. \tag{7}$$

In the experiments, a transfer function between the wavemaker stroke and the surface elevation was determined first and applied to Eq. (7) to obtain the input signal to the wavemaker. The overall amplitude of the input signal was adjusted so that one non-breaking and three breaking wave groups are achieved. Major breakers in these focusing groups are essentially plungers.

For the generation of wave groups subject to modulational instability, wave groups composed of a carrier wave and two side-band perturbation components are produced. The surface displacement at the wavemaker can be described by

$$\zeta(t) = a_0 \cos(\omega_0 t) + b \cos(\omega_1 t - \frac{\pi}{4}) + b \cos(\omega_2 t - \frac{\pi}{4}). \tag{8}$$

Here, $\omega_0$, $\omega_1$, and $\omega_2$ are the angular frequencies of the carrier wave, the lower and the upper side-band perturbations, respectively; $a_0$ and $b$ are the amplitudes of the carrier wave and the side-band perturbations, respectively. The initial phase of the side bands is set to $-\pi/4$ to meet the maximum growth condition.[9] The amplitude ratio, $b/a_0$ is set in the range from 0.3 to 0.5, depending on the specific wave group. To ensure that resonant wave interaction occurs for these gravity wave frequencies, the following conditions have to be satisfied:

$$2\omega_0 = \omega_1 + \omega_2, \tag{9}$$

$$\omega_{1,2} = \omega_0 \pm \Delta\omega/2, \tag{10}$$

$$0 < \frac{\Delta\omega}{\varepsilon\omega_0} \leq 2\sqrt{2}. \tag{11}$$

Here $\varepsilon = k_0 a_0$ and $k_0$ are the initial wave steepness and wavenumber of the carrier wave, respectively; $\Delta\omega$ is the frequency bandwidth. In the experiments, the frequency bandwidth is chosen carefully for given carrier wave frequency and wave steepness based on the results of Tulin and Waseda[11] (Figure 17) to achieve approximately the greatest growth rate. Details of the wave group parameters are given in Table II.

Similar to the generation of focusing wave groups, the actual input signal to the wavemaker is obtained by multiplying Eq. (8) with the transfer function. In addition, to avoid an abrupt motion of the wavemaker and the development of noise in the tank, such as the cross tank waves and reflected waves from the absorber,[11] a window function is applied and the wavemaker is set in motion for 3 min for each test run; however, data analysis is limited to measurements from the first 50 s during which the first wave probe measurement used for model initialization is free from reflected waves.

In the wave group generation, a differential TTL (transistor–transistor logic) signal corresponding to the initial motion of the wavemaker is also generated. This TTL signal is used to determine the surface elevation measurement time relative to the initial motion of the wavemaker (i.e., $t = 0$) and also to trigger a high-speed imager to capture surface profiles during active breaking.

TABLE II. Specified parameters for the wave groups subject to modulational instability. Note that BFI 1710 is a non-breaking group while the rest are breaking groups.

| Wave group | $f_0 = \omega_0 /2\pi$ (Hz) | $\Delta\omega/\omega_0$ | $\varepsilon = k_0 a_0$ |
|---|---|---|---|
| BFI 1710 | 1.7 | 0.166 | 0.10 |
| BFI 1712 | 1.7 | 0.200 | 0.12 |
| BFI 1716 | 1.7 | 0.266 | 0.16 |
| BFI 1720 | 1.7 | 0.330 | 0.20 |
| BFI 1616 | 1.6 | 0.266 | 0.16 |
| BFI 1620 | 1.6 | 0.330 | 0.20 |
| BFI 1516 | 1.5 | 0.266 | 0.16 |
| BFI 1520 | 1.5 | 0.330 | 0.20 |

### C. Surface elevation and profile measurements

A PC, two National Instrument data acquisition boards (USB-6221), and 14 capacitance wave probes (Akamina Technologies) are used to measure the surface elevation at wave stations along the tank. The first wave station is located 1.83 m downstream of the wavemaker. Note that the transitional effects of wave generation using a piston-type wavemaker are negligible approximately three water depths (1.86 m in this study) from the wavemaker.[12] The distance between two adjacent probes varies, but ranges from 60 cm to 85 cm. Specific locations of the probes relative to the mean position of the wavemaker are provided in (a) of Figure 2. The sampling rate is chosen as 100 Hz in the measurements. For each wave group, five repeated measurements are achieved and averaged to minimize error. Figure 2 provides two series of example time histories of the surface elevations.

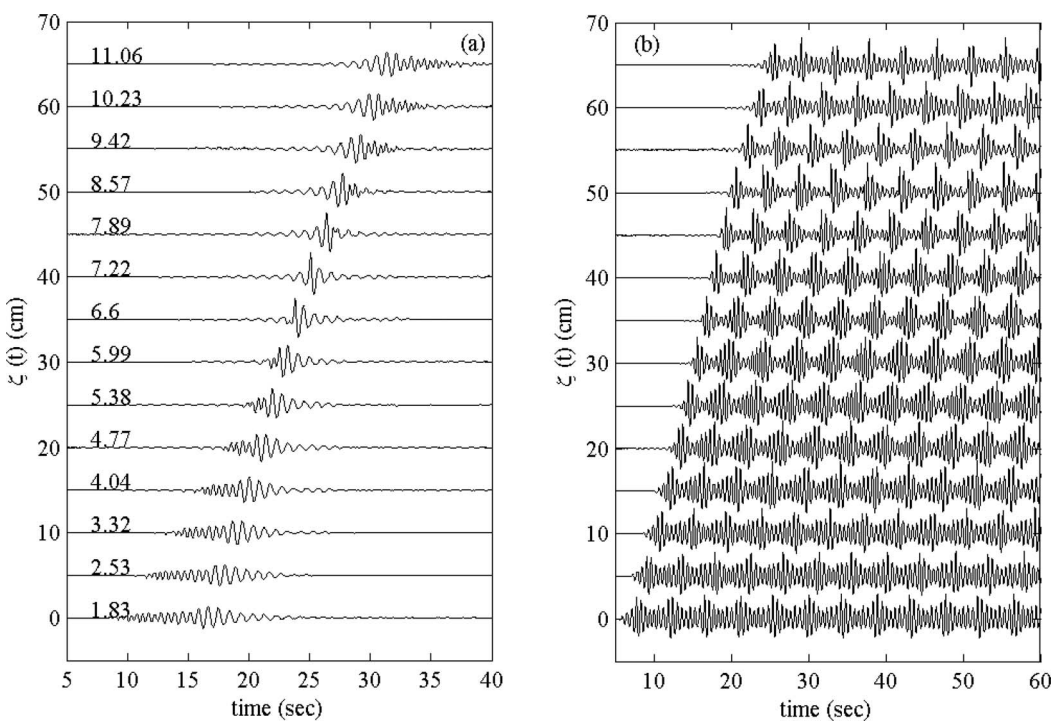


FIG. 2. Example time series of measured surface elevation of (a) a focusing group and (b) a group subject to modulational instability. Both groups lead to wave breaking. An offset of 5 cm is applied in the ordinates to separate measurements from different stations. Locations of the wave station relative to the wavemaker are shown in (a), e.g., 1.83 and 2.53 (m), and correspond to those in (b) also.

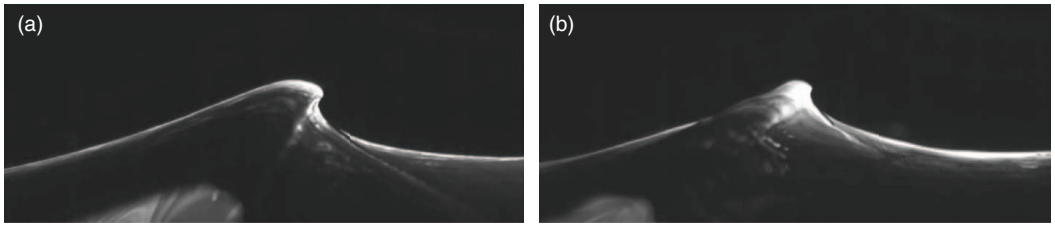


FIG. 3. Example images of the surface profiles of steep wave crests due to (a) energy focusing and (b) modulational instability. Both steep crests propagate from left to right and develop into plunging breakers subsequently.

For the measurement of local geometries of the breaking wave crests, a high-speed imager (Phantom V9.1 with 12 GB internal memory) is used to capture the surface profiles during active wave breaking. The imager, equipped with a 55 mm focal length Nikon lens, is positioned in front of the tank with its axis oriented slightly downwards for a better image of the field of view. Images are captured at 500 frames per second (fps). The size of the field of view depends on specific setups at different locations along the tank, but is approximately 84 cm long and 21 cm wide (1632×408 pixels). Using a precise planar target with known spacing, the spatial resolution is determined and the image distortion is shown to be negligible.

To facilitate the high-speed imaging, a 15 W DPSS laser is used as the light source for illumination. A thin laser light sheet is generated through a series of optics and is directed downward into the water, in which fluorescent dye (Rhodamine B) is dissolved to improve the illumination. Figure 1 provides an illustration of the setup and Figure 3 shows two example images captured during the experiments.

## III. LOCAL WAVE GEOMETRIES OF BREAKING WAVES

### A. Definitions

As shown in Figure 4, the wave crest height $H_C$, the wave trough height in front of the crest $H_{t1}$, and one behind the crest $H_{t2}$ are defined. The distance between two consecutive zero-crossing points adjacent to the crest tip, $L_C$, is used to determine a local wavelength, $L_b = 2L_C$, with which a local wavenumber and a local wave steepness can be computed, i.e., $k_b = 2\pi/L_b$ and $S_b = k_b(2H_C + H_{t1} + H_{t2})/4$, respectively. A local angular wave frequency, $\omega_b$, corresponding to the local wavenumber $k_b$ can then be determined using the linear dispersion relation. In addition, a wave asymmetry parameter is defined as $R_b = L_2/L_C$, where $L_2$ is the horizontal distance between the crest tip and the zero-crossing point immediately behind it.

For the estimation of the eddy viscosity with Eq. (4), the breaking time, $T_{br}$, the horizontal breaking length, $L_{br}$, and the falling crest height, $H_{br}$, associated with the breaking waves are also defined and details are referred to Introduction of this paper and the study by Tian *et al.*[6] Note that the breaking waves are all visually identified with the aid of high-speed imaging and that wave breaking inception is indicated by the presence of vertical wave crest fronts. Very small spilling breakers that cannot be easily detected by visual inspection are not considered. We also note that special attention shall be given to the falling crest height, $H_{br}$, originally defined in the scaling analysis of energy

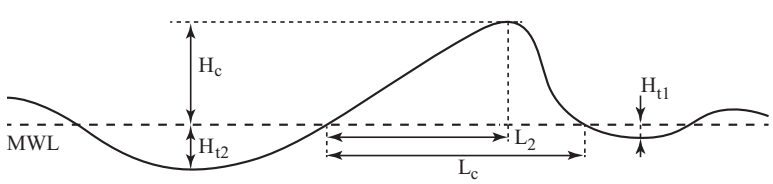


FIG. 4. Sketch of a steep wave crest and definitions of local wave parameters. The wave propagation direction is from left to right.

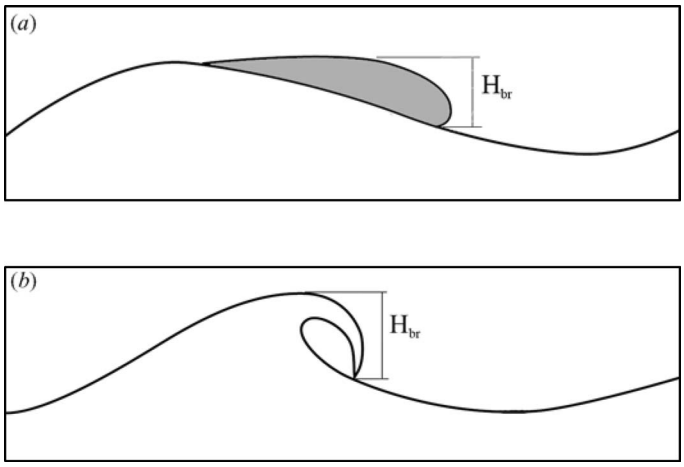


FIG. 5. Definition of the falling crest height, $H_{br}$ for (a) a spiller and (b) a plunger according to Drazen *et al.*[7]

dissipation by Drazen *et al.*[7] and shown here in Figure 5. As this definition is somewhat ambiguous for a spilling breaker, more discussion will be provided in Sec. III D.

### B. Wave crests approaching breaking

Wave crests approaching breaking are typically associated with local wave steepening, represented by wave crest growth and wavelength reduction. Figure 6 shows the growth of the wave crest, as well as the variation of surface elevation at the wave troughs preceding and following it, for three breakers. Prior to wave breaking, the crest height growth rates of the two plungers in (b) and (c) of the figure (due to modulational instability and energy focusing, respectively) are comparable and

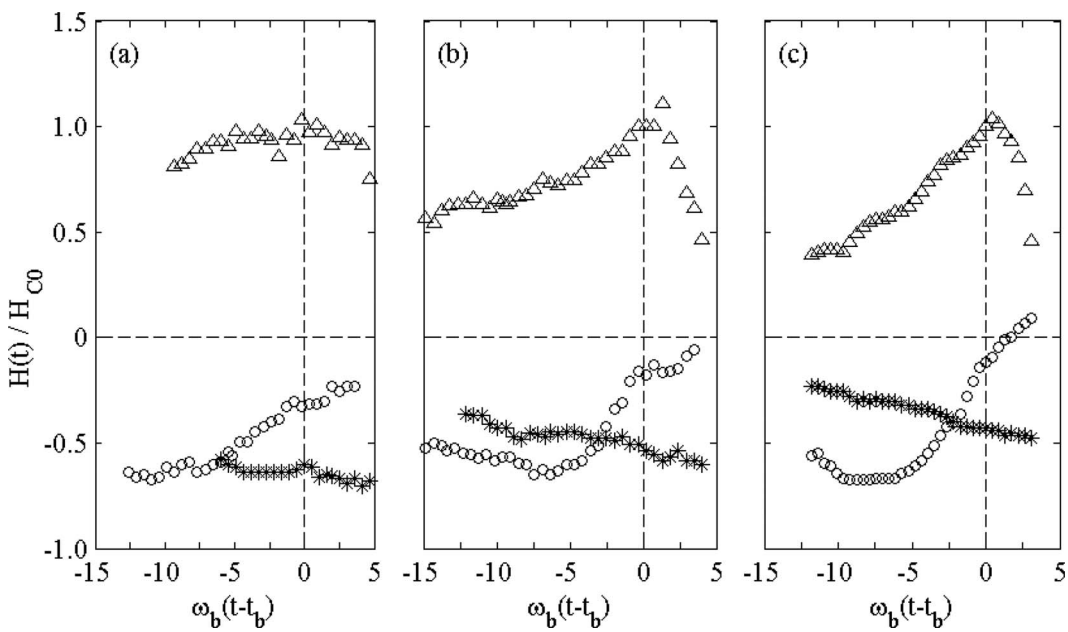


FIG. 6. Temporal evolution of the breaking wave crest height, (negative) height of the wave troughs of (a) a spiller and (b) a plunger due to modulational instability and (c) a plunger due to energy focusing. Triangles represent $H_C(t)/H_{C0}$; circles represent $H_{t1}(t)/H_{C0}$, and asterisks depict $H_{t2}(t)/H_{C0}$. Here $H_{C0}$ is the wave crest height at wave breaking, i.e., at $t-t_b = 0$. The relative time, $t-t_b$, is non-dimensionalized with the local angular wave frequency, $\omega_b$, at wave breaking.

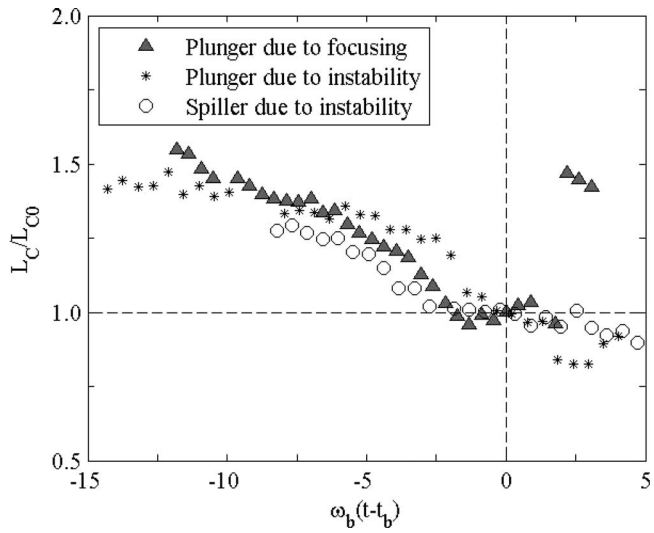


FIG. 7. Evolution of normalized $L_C$ as wave crests approach breaking. $L_{C0}$ is $L_C$ at wave breaking, where $t-t_b = 0$. Note that the wavelength of the plunger due to energy focusing (solid triangles) increased abruptly after breaking. This sudden increase is corresponding to the disappearance of one zero-crossing point due to the trough in front rising above the mean water level, as shown in (c) of Figure 6. This also causes the horizontal crest asymmetry parameter, $R_b$, to decrease to a very small value, as shown later in Figure 8. In this scenario, the wavelength should be redefined with the horizontal location of the wave trough in front rather than the next available zero-crossing point. The relative time, $t-t_b$, is non-dimensionalized with the local angular wave frequency, $\omega_b$, at wave breaking.

both are much greater than that of the spilling breaker shown in (a). The crest height of the spilling wave is much more uniform over time. The growth of the crest height of breaking waves was also observed in previous studies.[13,14] In fact, the latter study suggests that the crest height growth rate may be related to the breaking strength. Our observation showed higher growth rate for plungers than that for spillers, qualitatively consistent with the findings of Diorio *et al.*[14] Following wave breaking, the crest height of the plungers decreases rapidly, corresponding to a significant loss of potential energy; however, no abrupt decrease of the crest height is observed for the spiller.

As the wave crests approach breaking, for both spilling and plunging breakers, the following wave troughs become slightly deeper in general while the troughs preceding become shallower. In fact, the surface elevation at the preceding wave trough is elevated above the mean water level after wave breaking in some breaking cases. Our observations show that breaking wave crests are typically followed by deep wave troughs with shallower troughs in front. This demonstrates the strong asymmetry of the local wave geometries, which shall be considered in the definition of local wave steepness, e.g., $S_b$ in this study.

Evolution of the local wavelength is illustrated in Figure 7. Despite some variations at different stages of the evolution process, the overall wavelength reduction rates for all three breakers are comparable. We note in the figure that the wavelength of the plunger due to energy focusing increased abruptly after breaking. This sudden increase corresponds to the disappearance of one zero-crossing point due to the trough in front rising above the mean water level, as mentioned before and shown in (c) of Figure 6. In this scenario, the wavelength should be redefined with the horizontal location of the wave trough in front rather than the next available zero-crossing point. According to Figures 6 and 7, one may argue that the wavelength decrease is the dominant factor in the steepening of a crest that subsequently develops to a spiller breaker; on the other hand, both wavelength reduction and wave crest growth are significant as the crests evolve to plunging breakers.

We examine also the evolution of the wave asymmetry parameter, $R_b$. As is shown in Figure 8, $R_b$ increases slightly as the two wave crests that develop into plunging breakers evolve. For the spilling breaker, $R_b$ exhibits a similar trend although less obvious, despite some local fluctuations. In addition, the $R_b$'s of the plungers at breaking onset are greater than that of the spiller. This

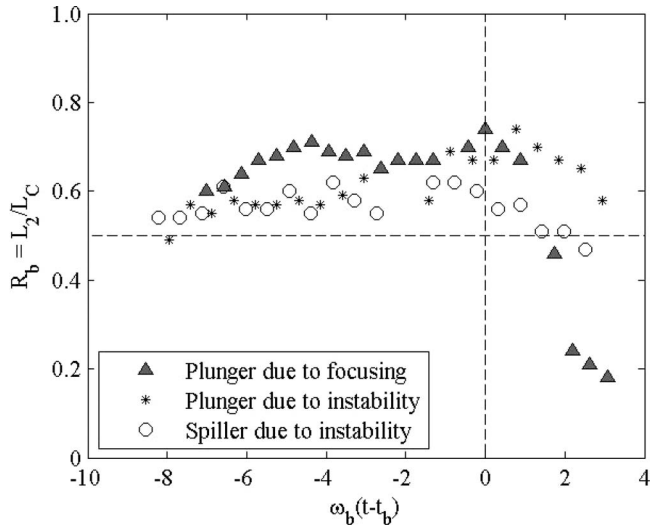


FIG. 8. Evolution of the wave asymmetry parameter, $R_b$, as wave crests approach breaking. $t_b$ represents the time associated with wave breaking. The relative time, $t-t_b$, is non-dimensionalized with the local angular wave frequency, $\omega_b$, at wave breaking.

observation is consistent with the experimental results of Bonmarin,[13] who reported a mean value of $L_2/(L_C-L_2)$ equal to 2.14 for typical plungers and 1.20 for typical spillers in his experiments, equivalent to $R_b = 0.68$ and 0.55, respectively.

### C. Breaking time and horizontal breaking length

With the definitions provided in Sec. III A, the pre-breaking parameters, i.e., $S_b$, $k_b$, and $\omega_b$, are determined at wave breaking onset and the post-breaking scales, $T_{br}$ and $L_{br}$, are measured from the high-speed imaging. Figure 9 provides a graphical summary of the results.

As shown in (a) and (b) of the Figure 9, the non-dimensional horizontal breaking length, $k_bL_{br}$ and breaking time, $\omega_bT_{br}$ depend on the local wave steepness $S_b$. These relationships appear to hold for breaking waves due to both modulational instability and energy focusing, though the non-dimensional breaking time seems to scatter slightly more than the non-dimensional horizontal breaking length. Another observation is that the minimum of the local steepness, $S_b$, of the breaking waves due to modulational instability is much greater than that of the breaking waves due to energy focusing. This may indicate that energy focusing may cause wave breaking at a smaller steepness than does modulational instability. However, this conclusion is based on limited data from breaking waves only. It has to be further evaluated by examining the maximum steepness of non-breaking waves in energy focusing wave groups and wave groups subject to modulational instability.

Figure 9(c) provides a rough estimation of the horizontal breaking crest propagation speed, $C_{br} = L_{br}/T_{br}$, relative to the local phase speed at breaking onset, $C_b = \omega_b/k_b$. The slope of the dash line is one, indicating $C_{br} = C_b$. For most of the spillers, $C_{br}$ is equal to or greater than $C_b$; while for most of the plungers, $C_{br}$ is smaller than $C_b$. This observation is not well understood.

### D. Falling crest height

As mentioned before, the falling crest height, $H_{br}$, originally defined and used in the scaling analysis of energy dissipation by Drazen *et al.*,[7] is somewhat ambiguous for spilling breakers. As shown in Figure 5, for a plunging breaker, $H_{br}$ is well defined and can be measured in experiments at a specific time, i.e., when the water jet emerging from the breaking crest just impacts the water surface beneath. For the plungers in our experiments, this impact typically occurs around 0.1 s after the initiation of wave breaking indicated by the presence of a vertical wave crest front.

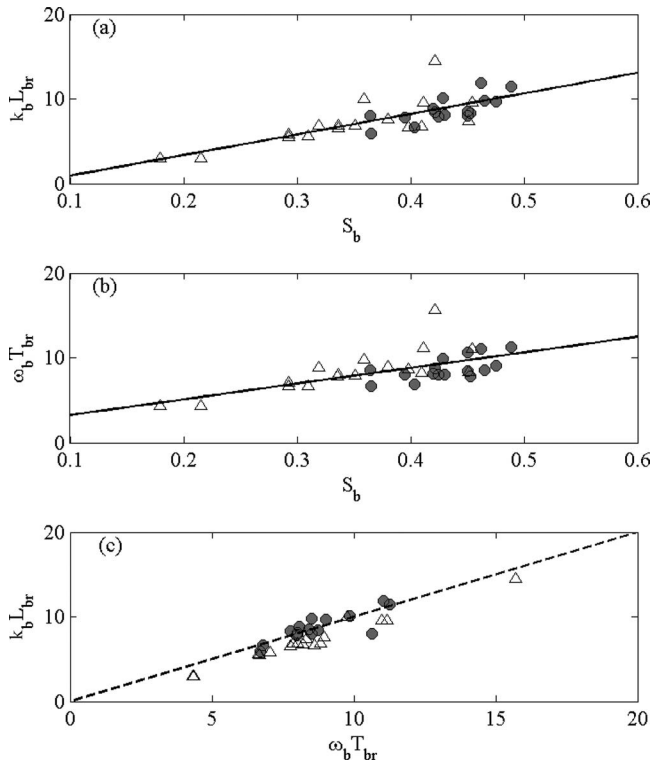


FIG. 9. Connection between pre- and post-breaking scales. (a) and (b) show $k_bL_{br}$ and $\omega_bT_{br}$ as a function of $S_b$, respectively; (c) can be used to estimate the breaking crest speed, $C_{br} = L_{br}/T_{br}$, relative to the local phase speed at breaking onset, $C_b = \omega_b/k_b$. Open triangles indicate results of breaking waves due to energy focusing (essentially plunging breakers), including results of the experiments in Tian *et al.*;[6] solid circles represent breaking waves due to modulational instability (most are spilling breakers). Solid lines in (a) and (b) represent linear least-squares fits and their equations are provided in Sec. IV B. The slope of the dash line in (c) is one, indicating $C_{br} = C_b$.

However, the timing to measure $H_{br}$ of spilling breakers is ill defined. Therefore, we choose somewhat arbitrarily to measure $H_{br}$ of the spilling breakers from 0.05 s to 0.15 s following the initiation of wave breaking. For a typical spiller, the variation of $H_{br}$ over this interval is not significant. However, for a spiller mixed with some plunging effects (see Bonmarin[13] for more detailed categorizations of breaking waves), $H_{br}$ during this period can vary dramatically. Nevertheless, a mean $H_{br}$ is determined by averaging measurements obtained during this time period.

We first examine the connection between the falling crest height and the local wave steepness, $S_b$, as provided in Figure 10(a). The results of the plungers, generated from both energy focusing and modulational instability, show reasonable dependence on the local wave steepness. Unfortunately, for a comparable $S_b$, $k_bH_{br}$ of the spillers is much smaller than the plungers and $S_b$ and $k_bH_{br}$ are less correlated. The data scatter in Figure 10(a) suggests that prediction of $H_{br}$ using $k_b$ and $S_b$ for both plungers and spillers is inappropriate. Therefore, alternative pre-breaking parameters will be considered.

It is noticed that a plunging breaker tends to have a greater wave asymmetry, $R_b = L_2/L_C$, than a spilling breaker. In fact, a similar observation had been made by Bonmarin,[13] who documented the minimum, the mean, and the maximum values of $L_2/(L_C - L_2)$ for the breaking waves observed in his study. For example, as mentioned before, a mean value of $R_b$ is determined to be 0.68 for typical plungers and 0.55 for typical spillers based on his measurements.

These observations suggest that the wave asymmetry may be related to the falling crest height. We plotted $k_bH_{br}$ against $R_b$ in Figure 10(b) and found better data collapse, although there is still noticeable data scatter. To the best of our knowledge, the correlation shown in Figure 10(b) has not been reported previously in others' studies.

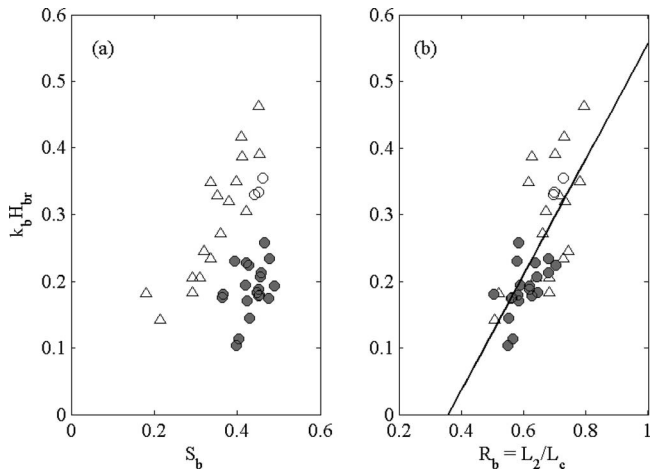


FIG. 10. Falling crest height, $k_bH_{br}$, as a function of (a) local steepness, $S_b$, and (b) the crest asymmetry parameter, $R_b$. Open symbols indicate results of breaking waves due to energy focusing (essentially plunging breakers), including results of the experiments in Tian *et al.*;[6] circles represent breaking waves due to modulational instability (open circles for plungers and solid ones for spillers).The solid line in (b) represents a linear least-squares fit and its equation is provided in Sec. IV B.

The correlations presented in (a) and (b) of Figure 9 and (b) of Figure 10 can be used to predict post-breaking time and length scales, i.e., $T_{br}$, $L_{br}$, and $H_{br}$, based on local wave parameters at wave breaking onset, i.e., $S_b$, $k_b$, $\omega_b$, and $R_b$. Predictions of the magnitude of the eddy viscosity, the temporal duration and the spatial region in which the eddy viscosity model is activated to forecast energy dissipation due to wave breaking in numerical simulations, are presented in Sec. IV.

## IV. NUMERICAL IMPLEMENTATION OF THE EDDY VISCOSITY MODEL

### A. Wave breaking criterion

Predicting wave breaking onset is one of the major challenges in the study of breaking waves. This prediction is usually based on wave steepness (e.g., Rapp and Melville[10]), wave crest kinematics, and/or energy focusing rate.[15–17] Previous studies[18,19] show that criteria based on wave crest geometry and kinematics may not be universal due to either the inapplicability of the criterion or the ambiguity in the definition of the wave parameters involved. On the other hand, the energy focusing rate based criteria appear to be very promising;[16,17] however, the criteria involve complicated processes to construct the predictive parameter, and its application in numerical simulations may be limited.

Considering that the wave crest turns over for plunging breakers, and that the local surface elevation becomes very steep, even vertical[14,20] in incipient spilling breakers, one may argue that the surface slope can be used to indicate breaking onset. In fact, in the numerical simulations by Babanin *et al.*,[21] the presence of a vertical water surface is used as a criterion for wave breaking.

In this study, we use a simple criterion based on *local surface elevation slope*, the spatial derivative of the surface elevation (*surface slope* for simplicity). Note that the spatial derivative of the surface elevation is negative on the leading side of the wave crest; therefore, a negative sign is used in the definition for convenience, i.e., $S = -\partial\zeta/\partial x$. $S$ can theoretically become infinite (and then change sign) as waves approach breaking, leading to a numerical singularity in simulations. Therefore, it is necessary to activate the eddy viscosity model before this happens, or, equivalently, when $S$ reaches a critical value, $S_C = (-\partial\zeta/\partial x)_C$, to avert numerical disaster.

Our previous study had determined a critical surface slope, $S_C = 0.95$, for breaking onset prediction.[22] The numerical simulations were carried out with initial conditions generated with surface elevations of non-breaking wave groups and linear wave theory. The overall amplitude of the non-breaking surface elevations are then increased gradually by multiplying by a gain factor until the numerical simulation fails, presumably corresponding to physical wave breaking. Maximum surface slope, within a few time steps before the formation of the numerical singularity, is recorded

and examined. According to the numerical tests, a critical surface slope, $S_C = 0.95$, is chosen to predict wave breaking onset in our numerical simulations. In other words, once the surface slope reaches this value, we assume that it continues to increase so that wave breaking occurs. Details regarding the determination of the critical surface slope can be found in the reference and, for the completeness of this study, a brief description and the key results are provided in Appendix.

In this study, numerical experiments using $S_C = 0.95$ are conducted for the breaking wave groups and are discussed in Secs. IV C–IV D. We found that numerical failures can be effectively prevented when activating the improved eddy viscosity model at this criticality. To test its sensitivity on numerical solutions, critical surface slopes of different values, i.e., $S_C = 0.9$, 1.0, and 1.05, are tested with two strong breaking groups (EF4 and BFI1720). It is found that $S_C = 0.9$ and 1.0 prevent the numerical disasters for both cases, but $S_C = 1.05$ does not. We also examined the results of the numerical tests using $S_C = 0.9$, 0.95 and 1.0 and found that the difference among the predicted total energy dissipation, as well as the surface elevation after breaking, is negligible. Therefore, to be consistent, the critical surface slope, $S_C = 0.95$, is chosen for wave breaking onset in our numerical simulations in this study.

### B. Eddy viscosity estimation

In our numerical simulations, local wave parameters, i.e., $S_b$, $k_b$, $\omega_b$, and $R_b$, are determined with the simulated surface profile when the surface slope just exceeds the critical value. Then the post-breaking time and length scales, i.e., $T_{br}$, $L_{br}$, and $H_{br}$, are predicted with

$$k_b L_{br} = 24.3 S_b - 1.5, \tag{12}$$

$$\omega_b T_{br} = 18.4 S_b + 1.4, \tag{13}$$

$$k_b H_{br} = 0.87 R_b - 0.3, \tag{14}$$

which are determined from the experimental data shown in (a) and (b) of Figure 9 and (b) of Figure 10 using linear least-squares fit, respectively. With these predictions, the eddy viscosity model is implemented for the numerical simulations using the following procedure.

When the local surface slope just exceeds the critical surface slope, $S_C = 0.95$, the breaking time and length scales, $T_{br}$, $L_{br}$, and $H_{br}$, are predicted using the local wave parameters, $k_b$, $\omega_b$, $S_b$, and $R_b$, determined with the simulated surface profile and Eqs. (12)–(14). Once $T_{br}$, $L_{br}$, and $H_{br}$ are predicted, a constant eddy viscosity is estimated with Eq. (4) and applied to a spatial domain of length $L_{br}$ starting from the location of the breaking crest tip for a temporal duration of $T_{br}$ from the time when $S$ just exceeds the criticality.

However, one should pay attention to the fact that, for some breaking waves, the trough in front of a breaking crest may rise above the mean water level, causing the zero-down crossing point between the trough and the crest to disappear. Notice that $L_C$ is defined as the distance between two consecutive zero-crossing points to each side of the breaking crest. When the preceding zero-crossing point vanishes, $L_C$ will be increased significantly and abruptly, as shown in Figure 7. This also causes the horizontal crest asymmetry parameter, $R_b$, to decrease to a very small value, as shown Figure 8. Therefore, under these conditions, $L_C$ is redefined as the distance between the zero-crossing point behind the breaking crest and the horizontal location of the trough in front. In addition, the minimum value of $R_b$ is set to be 0.5, which is the value for sinusoidal waves.

### C. Numerical simulation results

The improved eddy viscosity model is incorporated into the pseudo-spectral model to simulate the evolution of two-dimensional breaking waves. In the code, the right-hand sides of Eqs. (2) were truncated to the fifth order and the nonlinear evolution equations of the system were solved

numerically with a pseudo-spectral method based on the fast Fourier transform (FFT) and a fourth-order Runge–Kutta method to integrate in time.

### *1. Energy focusing wave groups*

Simulations of the energy focusing wave groups are conducted in a numerical wave tank 50 m long with the domain from 20 to 35 m corresponding to the physical wave tank. The numerical domain is discretized with $2^{12}$ points and a time step of 0.01 s is used in the simulations. The simulation period, $T$, is 40.95 s, which is of sufficient duration for the wave groups to completely pass the last wave station.

Using linear wave theory, initial conditions, i.e., spatial variation of the surface profiles and velocity potentials (from 0 to 20 m in the numerical domain) at the mean water level, are generated with surface elevation measurements at the first wave probe located at 1.83 m (i.e., 21.83 m in the numerical domain). To match the surface elevation measured at the first wave probe, the linear model without viscous effects is solved over the spatial domain from 0 to 21.83 m; a similar strategy is also used in Tian *et al.*[6] In the remainder of the numerical tank, the fifth order model with the improved eddy viscosity model is solved. A transition layer is applied from 21.83 to 22.08 m to avoid any transition irregularity of the surface profiles.

For the non-breaking wave group (i.e., EF 1), in the viscous domain, an equivalent kinematic viscosity, $\nu_{eqv} = 5 \times 10^{-6}\mathrm{m}^2\mathrm{s}^{-1}$ is applied to the surface boundary conditions (to account for the free surface damping and the frictional loss due to tank side walls and bottom). The equivalent kinematic viscosity is determined such that the total potential energy predicted in the simulations matches the experimental measurements, as shown in Figure 11. For the breaking wave groups, the same equivalent kinematic viscosity is used in the absence of wave breaking. When breaking occurs, the code automatically detects the breaking crests and activates the improved eddy viscosity model to dissipate energy.

Figure 11 provides a comparison of the predicted and measured long time integration of the surface variance, which is proportional to the total energy passing a wave station according to linear

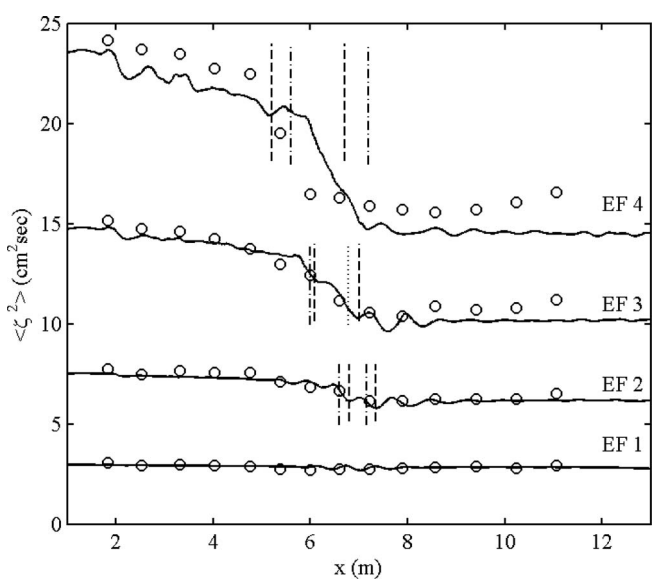


FIG. 11. A comparison of the long time integration of the surface variance, $\langle\zeta^2\rangle = \int_0^T \zeta(x,t)^2 dt$, for the four energy focusing wave groups (Group EF 1 is a non-breaking one, the rest are breaking ones). Here, $T = 40.95$ s. According to linear wave theory, the integration is proportional to the total energy passing a wave station. Symbols are experimental measurements and solid lines are numerical results. Dash lines indicate the breaking regions of the major breaking events in experiments; Dash-dot lines are for those predicted in the simulations. Note that the shown breaking regions are for the major breaking events only; locations of secondary breaking prior and/or subsequent to the major ones are not indicated.

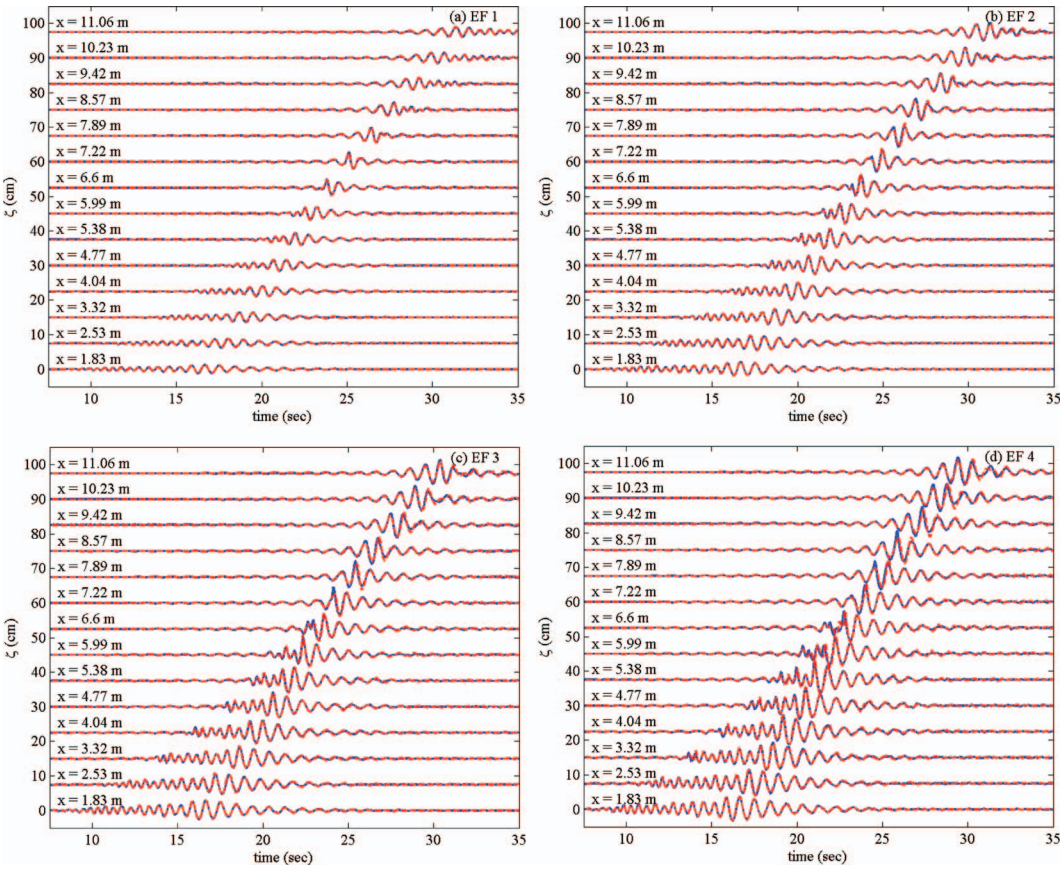


FIG. 12. (Color online) (a)–(d) present the surface elevation at wave stations along the tank. Wave group EF 1 is non-breaking, the rest are breaking cases. Solid lines are measured and dash lines are predicted. Locations of the wave stations are provided in the figure, e.g., $x = 1.83$ m. For clarity, an offset of 7.5 cm is applied to the ordinate to separate the surface elevations at different stations.

wave theory. Clearly, the total potential energy as a function of space for both non-breaking and breaking wave groups are predicted well in the simulations. The results indicate that the improved eddy viscosity model simulates well the total energy dissipation in the breaking events. In addition, as shown in (a) to (d) of Figure 12, the computed surface elevation downstream of the wave breaking region matches well the measurement, though the comparison for wave group EF 4 (the most violent breaking case) is not as good as the others. This is possibly due to both the simple model itself and the initial conditions that are generated with linear wave theory. Overall, the improved eddy viscosity model does a great job in predicting both energy dissipation in breaking events and the surface elevation downstream of breaking for the focusing wave groups.

### *2. Wave groups subject to modulational instability*

Simulations of the wave groups subject to modulational instability are performed in a 50 m long numerical tank where the domain from 25 to 40 m corresponds to the physical wave tank. The remaining numerical setups in the simulations are similar to those of the focusing wave groups. Simulations are conducted for wave groups with center frequency of 1.7 Hz while the simulation period, $T$, is limited to 50 s. Note that in the experiments, it takes approximately 50 s for the wave front to propagate to the wave absorber and then return to the wavemaker following reflection.

Figure 13 presents a comparison of the long time integration of the surface variance. We point out that the decrease of this long time integration (proportional to the total energy) is mainly due to two factors. One is energy dissipation in breaking events; the other is that, since the integration

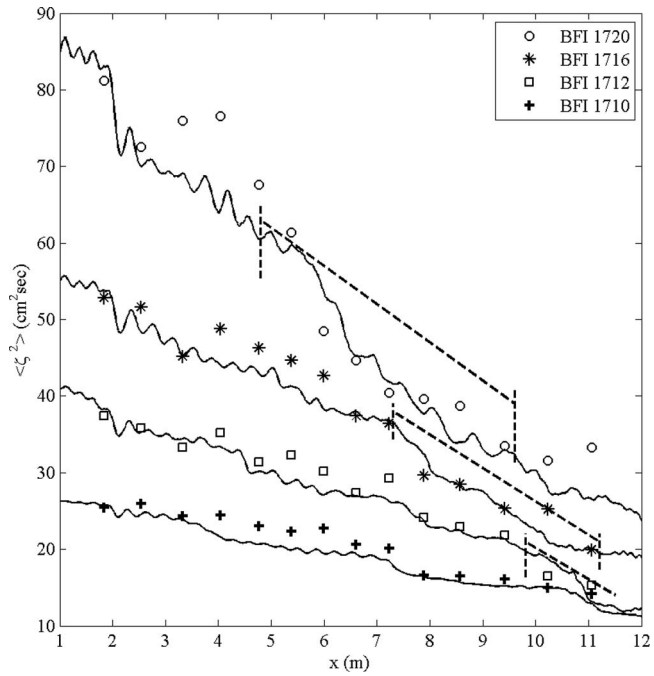


FIG. 13. Comparison of the long time integration of the surface variance, $\langle \zeta^2 \rangle = \int_0^T \zeta(x,t)^2 dt$, for the wave groups subject to modulational instability. Here, $T = 50$ s. According to linear wave theory, the integration is proportional to the total energy passing a wave station. Symbols are experimental measurements and solid lines are numerical results. Note that for the BFI 1712 comparison, once breaking ensued, it continued to the downstream extent of the tank. Regions in which wave breaking was observed in the experiments are highlighted with the dash lines. Note that the decrease of the integration (total energy) is mainly due to two factors. One is energy dissipation in breaking events; the other is that, since the integration is limited from 0 to 50 s, not all generated waves upstream have arrived at the downstream wave station yet (see Figure 14).

is limited from 0 to 50 s, not all generated waves upstream have reached the downstream wave stations. For both the non-breaking and the breaking wave groups, the total energy as a function of space is predicted reasonably well, especially considering that multiple breakers occurred at different locations repeatedly and/or simultaneously in the physical experiments for some breaking groups. The results suggest that the improved eddy viscosity model simulates well the total energy dissipation due to wave breaking.

The surface elevation is simulated relatively well for the non-breaking case (a), although some minor disparity can still be found for surface elevations measured far downstream. However, obvious disagreement between the predicted and the measured surface elevation after wave breaking is observed, as shown in (b) of Figure 14. The prediction for the breaking group (e.g., BFI 1720) is good to wave breaking. (Note that the breaking region is roughly from $x = 4.8$ m to 9.6 m, in which wave breaking occurs at different locations repeatedly and/or simultaneously for this group.) The predicted surface elevation disagreement becomes noticeable from roughly $x = 6.6$ m. As the breaking wave group propagates further downstream, significant disparity is observed. This result is inconsistent with the energy focusing wave groups, for which both total energy dissipation and the surface elevation after wave breaking are well simulated. Possible causes of the poor surface elevation prediction for the modulated breaking wave groups are discussed in Sec. IV D.

### D. Discussion

A few possible causes for the disagreement of the predicted and measured surface elevation observed for wave groups subject to modulational instability are presented and discussed. In our numerical simulations, a wave breaking criterion, a scheme to estimate the eddy viscosity and its implementation in the code, and initial conditions are required. Therefore, these factors will

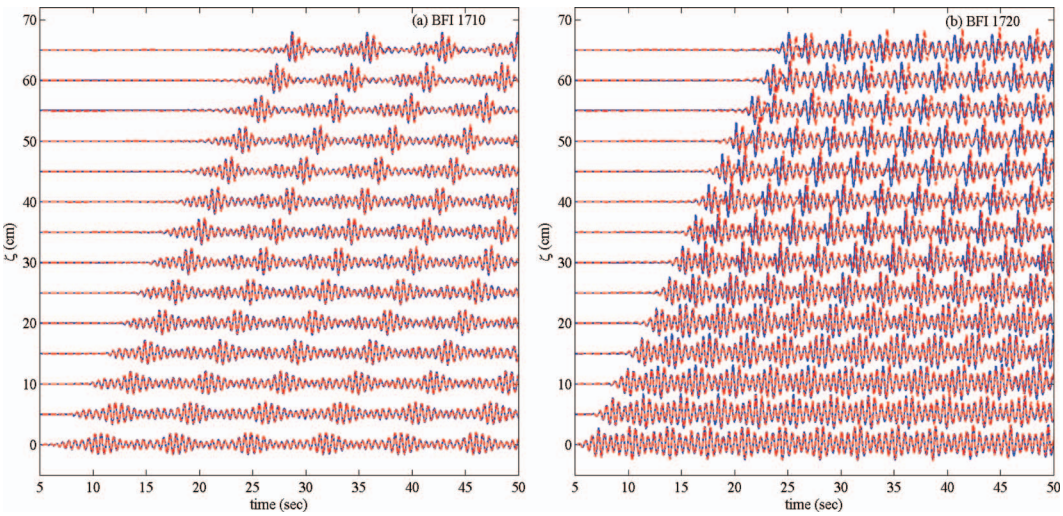


FIG. 14. (Color online) (a) and (b) present the measured (solid lines) and the predicted (dash lines) surface elevation at different wave stations along the tank. Locations of wave stations are the same as those shown in Figure 12. For clarity, an offset of 5 cm is applied to the ordinate to separate the surface elevations at different stations.

be discussed and examined individually. To facilitate the examination, a breaking wave group (i.e., BFI1712) that has several spilling breakers far downstream of the wavemaker is used in the numerical experiments.

We first examine the wave-breaking criterion. The critical surface slope for breaking onset prediction is increased from 0.95 to 1.05, 1.15, and 1.25 in the test. We found that $S_C = 1.25$ cannot prevent the code from blowing-up for this wave group (BFI 1712). Both $S_C = 1.05$ and 1.15 can prevent numerical disaster with the predicted total energy loss and the surface elevation after breaking virtually the same. In addition, the variation of the predicted incipient breaking location using $S_C = 0.95$, 1.05, and 1.15 is within 0.15 $\lambda_c$, where $\lambda_c$ is the wavelength of the carrier wave. (Note that the observed first breaker is about one wavelength, $\lambda_c$, downstream of that predicted.) The test shows that the critical surface slope is unlikely the cause of the poor surface elevation prediction for the modulated breaking wave group.

A second test that addresses the eddy viscosity estimation is conducted. The eddy viscosity is estimated through Eq. (4), in which the breaking time and length scales, $T_{br}$, $L_{br}$, and $H_{br}$, have to be predicted first using Eqs. (12)–(14). For this modulated wave group (i.e., BFI 1712), the breakers are mainly spillers or, at least, not typical plungers. We questioned whether using the empirical formulae (12) to (14) caused an overestimation of the eddy viscosity for the spillers. Therefore, we determined two additional linear least-sqaures best fits using only the measured horizontal breaking length, $L_{br}$, and breaking time, $T_{br}$, of the spillers, similar to Eqs. (12) and (13), respectively. In addition, data for the spillers shown in (a) and (b) of Figure 10 are used to determine another two best fits for the measured vertical length, $H_{br}$, i.e., $k_b H_{br}$ as a function of $S_b$ and $R_b$, respectively. We applied these new best fits to the code and conducted numerical tests. We found that the variation in the predicted eddy viscosity can be over 80%; however, the predicted total energy loss and surface elevation after breaking are again close to each other since $L_{br}$ and $T_{br}$ are also different from the previous estimates. This demonstrates that our model is not sensitive to the eddy viscosity estimation, presumably as it is implemented locally in a short region and for a short period. Hence the disparity between the measured and the predicted surface elevation following breaking may not be attributed primarily to the eddy viscosity estimation.

It is also possible that the detailed implementation scheme of the eddy viscosity model may cause the disagreement. We predicted the breaking time and length scales, $T_{br}$, $L_{br}$, and $H_{br}$, based on pre-breaking wave parameters, $k_b$, $\omega_b$, $S_b$, and $R_b$. Once $T_{br}$, $L_{br}$, and $H_{br}$ are predicted, the estimated, constant eddy viscosity is applied to a spatial domain of length $L_{br}$ starting from the location of the breaking crest tip for a temporal duration of $T_{br}$ from the time when $S$ just exceeds $S_C$. Therefore, the

breaking region $L_{br}$ is fixed for a given breaking event. At the initial stage of the breaking, waves in front of the actual breaking crest may be located within the estimated breaking region. In addition, at the final stage of breaking, waves behind the actual breaking crest may have already entered the breaking region. Since a constant eddy viscosity is applied throughout the breaking process, the model may have incorrectly dissipated energy from steep non-breaking waves. The implementation scheme of the eddy viscosity model may be improved and its performance will be evaluated in future studies.

We should also comment on the generation of initial conditions. The initial conditions used in the numerical simulations are generated with upstream wave probe measurements and linear wave theory. Obviously, for strongly nonlinear wave groups, error in the generated initial condition for the velocity potential may be sufficiently large that it could render the subsequent surface elevation prediction inaccurate. A similar initialization technique was adopted in Goullet and Choi[3] to study the evolution of nonlinear irregular waves and was found to be reliable. Considering that the linear velocity potential is accurate to the third order in wave steepness, the initialization technique based on linear theory might be reasonable. In addition, the location of the first wave probe whose measurement is used to initialize the numerical model is close to the wave maker and we expect nonlinearity to play little role in the intervening region. Therefore, an error in our initialization technique appears to be minor, as can be seen in Sec. V. Nevertheless, the nonlinear effects should be examined carefully in future studies.

Uncertainties in laboratory experiments may also have contributed to the discrepancy between the prediction and the measurement. Because of the width of the two-dimensional wave tank, three-dimensionality may be non-negligible, in particular, when wave breaking occurs. In addition, to investigate the significance of wave reflection, a time domain method for separation of incident and reflected waves is used to determine the magnitude of the reflected waves.[23] With the surface elevation measured at three probes, the reflected total wave energy is determined as more than 5% of the total incident wave energy, which gives an equivalent reflection coefficient as high as 20%. Wave reflection is not considered in the numerical simulations and the possible presence of a significant amount of wave reflection in the experiments along with three-dimensionality may have contributed to the disagreement between the measurement and the prediction.

Furthermore, the application of the model assumes that the dissipated energy in a breaking event is mainly consumed by turbulence generation and is eventually transferred to heat through viscosity, but physical processes other than the generation of turbulence also dissipate wave energy in a breaking event. Air entrainment, especially for plunging breakers, can account for up to 50% of the total energy dissipated due to wave breaking.[24] Breaking waves also transport energy from the breaking location by generating currents and both upstream and downstream propagating waves (e.g., Rapp and Melville[10]). These effects are not considered in the development of this eddy viscosity model and may have to be considered in further studies.

## V. APPLICATION OF THE EDDY VISCOSITY MODEL TO IRREGULAR WAVES

To test its applicability to irregular waves of broadband spectrum (therefore, to ocean waves), the pseudo-spectral model combined with the eddy viscosity model is used to solve numerically for the evolution of long-crested irregular waves. Since the two-dimensional wave tank at KAIST used to develop the eddy viscosity model is too short to generate broadband irregular waves, our numerical solutions are compared with additional laboratory experiments conducted in a rectangular basin at the Institute for Ocean Technology in Newfoundland, Canada. As described in Goullet and Choi,[3] the wave basin is 75 m long and the surface elevation was measured using 20 wave probes of capacitance type with a sampling rate of 0.02 s. The wave probes were equally spaced over a distance of 22.8 m with the first wave probe located 17.8 m (equivalent to 11.4 peak wavelengths) from the wavemaker. To generate irregular waves, the motion of a piston-type wavemaker was characterized by the JONSWAP spectrum:

$$S_\omega(\omega) = \frac{5}{16}\frac{\omega_p^4 H_s^2}{\omega^5}\exp\left[-\frac{5}{4}\left(\frac{\omega_p}{\omega}\right)^4\right]\gamma^{exp\left[-(\omega-\omega_p)^2/2\sigma^2\omega_p^2\right]},$$

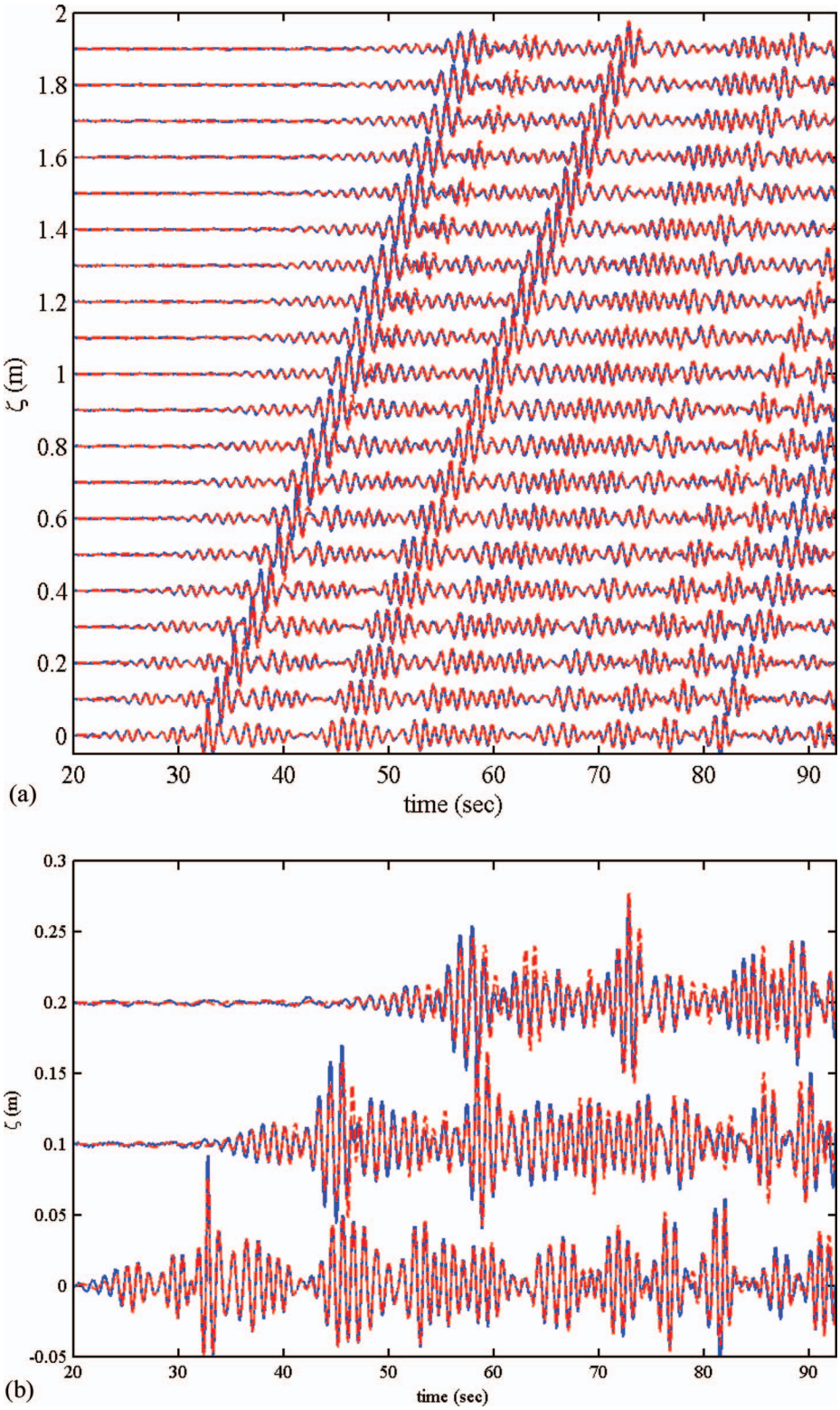


FIG. 15. (Color online) Evolution of long-crested irregular waves characterized by the JONSWAP spectrum with $H_s = 0.12$ m, $f_p = 1$ Hz, and $\gamma = 3.3$: (a) Comparison between the measured (solid lines) and the predicted (dashed lines) surface elevations at 20 different wave stations along the tank. For clarity, an offset of 10 cm is applied to the ordinate to separate the surface elevations at different stations; (b) Detailed comparison at the 1st, 10th, and 20th wave stations located at $x/\lambda_p = 0$, 6.92, and 14.62 (from bottom to top).

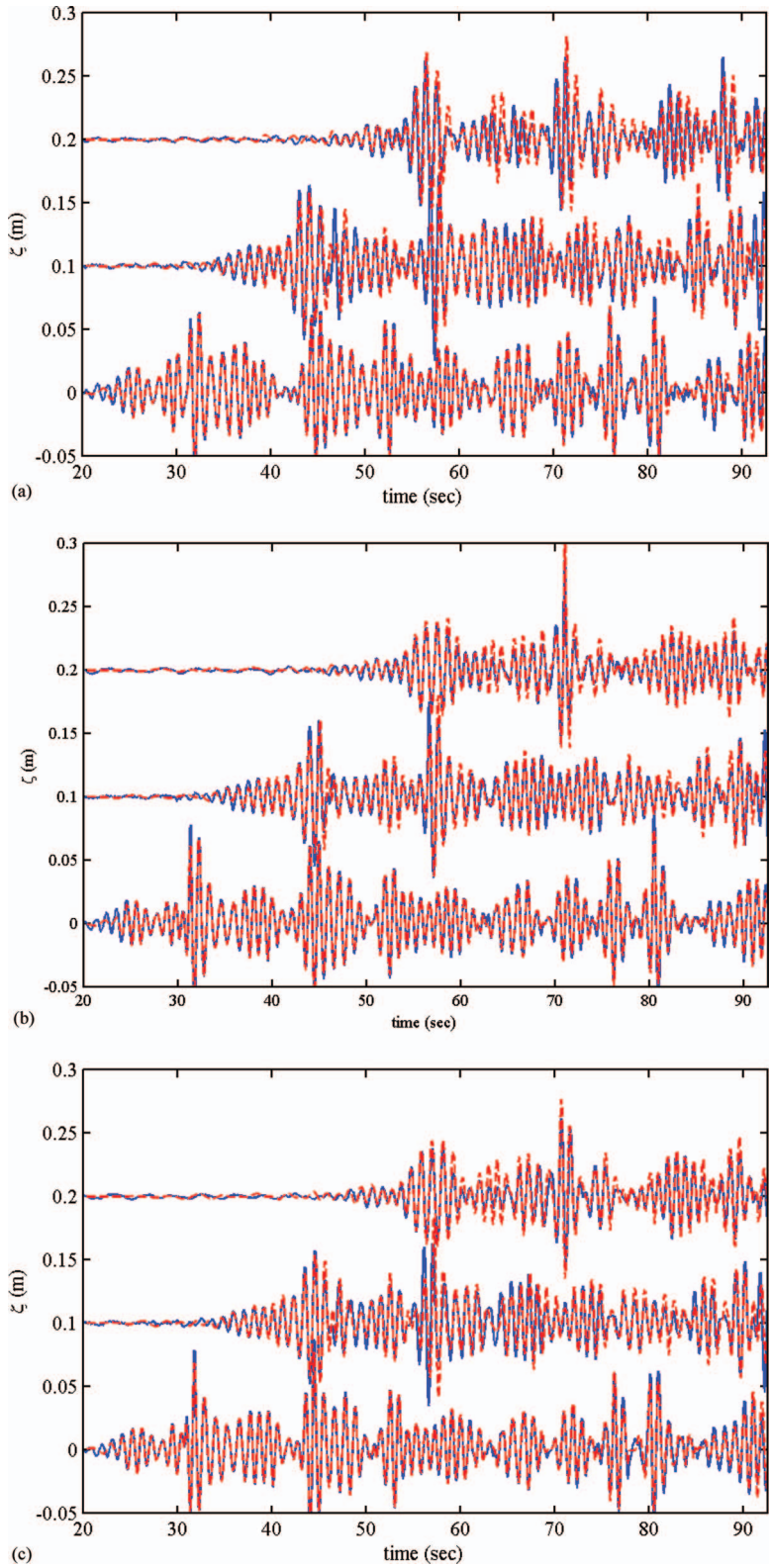


FIG. 16. (Color online) Comparison between the measured (solid lines) and the predicted (dashed lines) surface elevations at the 1st, 10th, and 20th wave stations wave stations (from bottom to top) along the tank for the evolution of long-crested irregular waves characterized by the JONSWAP spectrum with $f_p = 1$ Hz. Other physical parameters are (a) $H_s = 0.14$ m and $\gamma = 3.3$; (b) $H_s = 0.12$ m and $\gamma = 20$; and (c) $H_s = 0.14$ m and $\gamma = 20$.

where $\omega_p$ is the peak frequency, $H_s$ is the significant wave height, $\gamma$ is the peak enhancement factor, and $\sigma$ is a function of wave frequency defined by $\sigma = 0.07$ for $\omega < \omega_p$ while $\sigma = 0.09$ for $\omega > \omega_p$. In our experiments, we have chosen the peak frequency of $f_p = 2\pi\omega_p = 1$ Hz, for which the corresponding wavelength is $\lambda_p = 1.56$ m, and two different values for the peak enhancement factor of $\gamma = 3.3$ and $\gamma = 20$. To validate the (inviscid) pseudo-spectral model, Goullet and Choi[3] used a data set for $H_s = 0.1$ m for which no wave breaking is observed. Notice that the corresponding wave steepness is given by $H_s/(2\lambda_p) = 0.032$. In the absence of wave breaking, the pseudo-spectral model was shown to predict the evolution of nonlinear irregular waves accurately to the downstream probe location at $x/\lambda_p = 14.62$. Although the comparison with laboratory measurements improves as the order of nonlinearity increases, it was shown[3] that the pseudo-spectral model truncated at the fifth order is found to yield satisfactory comparison.

To validate the pseudo-spectral model with eddy viscosity, we adopt data sets for $H_s = 0.12$ m and $H_s = 0.14$ m, for which single/multiple wave breakers are detected numerically and, therefore, the (inviscid) pseudo-spectral model is inapplicable. As shown in Figure 15, for the case of $H_s = 0.12$ m and $\gamma = 3.3$, the onset of a single breaking event is detected approximately at $x = 6.2$ m ($x/\lambda_p = 3.97$) from the first wave probe, but the predicted and measured surface elevations compare well beyond the incipient breaking location. As the significant wave height is increased to $H_s = 0.14$ m, the corresponding wave field becomes more nonlinear and, therefore, a slightly larger discrepancy than the case of $H_s = 0.12$ m is noticed in Figure 16(a). Nevertheless, the eddy viscosity model predicts reasonably well the evolution of irregular waves downstream of the active breaking region between $x = 11.1$ m and 12.7 m.

As the spectral bandwidth is decreased (or, equivalently, $\gamma$ is increased to 20), it is well known (e.g., Goullet and Choi[3]) that stronger wave focusing occurs and, therefore, multiple breakers are expected to be observed. As shown in Figures 16(b) and 16(c), although our numerical simulations detect multiple breakers approximately at $x = 2.2$ m, 5.2 m, and 22.2 m for $H_s = 0.12$ m and at $x = 6.2$ m and 24.2 m for $H_s = 0.14$ m from the first wave probe, the pseudo-spectral model with eddy viscosity predicts well the evolution of such highly nonlinear waves. In particular, the prediction of the time when the highest peak appears at the last wave station located at $x = 22.8$ m is surprisingly good even though the numerical solutions over-predict slightly the peak wave amplitudes.

## VI. CONCLUSIONS

In this study, an improved eddy viscosity model to simulate energy dissipation in two-dimensional breaking waves is developed and evaluated with experimental results. This model along with a breaking criterion based on a critical surface slope detects automatically wave breaking onset, determines local wave parameters just prior to wave breaking, predicts post-breaking time and length scales, and estimates the eddy viscosity to simulate energy dissipation due to wave breaking. It is found that this model predicts well the total energy dissipated in breaking waves.

For further development, two-dimensional wave breaking experiments are conducted in which breaking waves are generated with both energy focusing and modulational instability. Surface elevations at different stations along the tank are measured with capacitance wave probes; surface profiles during active wave breaking are captured from a high-speed camera. Local wave geometries of the wave crest are defined and determined with the high-speed imaging results. Evolution of the wave parameters as wave crests approach breaking is examined. We found that a breaking crest is typically followed by a deep trough with a shallow trough in front. It is also found that both wavelength decrease and wave crest growth are significant as the crest develops to a plunging breaker; on the other hand, wavelength reduction is the dominant factor in the steepening of a wave crest that subsequently evolves to a spilling breaker.

Post-breaking time and length scales are defined and determined in this study. The breaking time and horizontal breaking length scale, $T_{br}$ and $L_{br}$, when properly non-dimensionalized, demonstrate strong dependence on the local wave steepness prior to wave breaking, $S_b$. The non-dimensionalized falling crest height, $k_b H_{br}$, is shown to be related to the wave asymmetry parameter, $R_b$. To the best of our knowledge, this finding has not been reported previously in others' studies.

A critical surface slope, $S_C = 0.95$, is identified through numerical experiments and adopted in our eddy viscosity model for wave breaking onset prediction. With the breaking criterion and the aforementioned correlations between the pre- and post-breaking wave parameters, the eddy viscosity model is capable of detecting automatically wave breaking onset and predicting eddy viscosity to simulate energy dissipation due to wave breaking.

Numerical simulations with the improved model are performed and compared to the experiments. It is found that the model predicts well the total energy dissipated in breaking events. In addition, the computed surface elevations following wave breaking agree reasonably well with the measurements for the energy focusing wave groups. However, for breaking wave groups due to modulational instability with spilling breakers, the surface elevation predictions compare less satisfactorily to experimental results, possibly, due to three-dimensionality and wave reflection in the experiments. The model is further validated with additional independent experimental measurements for highly nonlinear irregular waves and the comparison for the surface elevation after wave breaking is satisfactory. The eddy viscosity model still should be improved by taking into account the effects of three-dimensional wave breaking and, possibly, allowing a dynamic (rather than constant) eddy viscosity during the breaking process, as discussed earlier.

## ACKNOWLEDGMENTS

W.C. and Z.T. gratefully acknowledge the support from the National Research Foundation of Korea funded by the ministry of Education, Science, and Technology through the WCU program (Grant No. R31-2008-000-10045-0). The laboratory experiments at the Institute for Ocean Technology in Newfoundland, Canada were supported by the US Office of Naval Research (ONR) through Grant No. N00014-05-1-0537 and W.C. thanks Okey Nwogu and Lawrence Mak for their help in setting up the experiments.

## APPENDIX: DETERMINATION OF THE CRITICAL SURFACE SLOPE

To determine $S_C = (-\partial\zeta/\partial x)_C$, we conducted a series of numerical experiments in which the right-hand sides of Eqs. (1) were truncated to the fifth order and the nonlinear evolution equations of the system were solved numerically with a pseudo-spectral method based on the fast Fourier transform (FFT) and a fourth-order Runge–Kutta method to integrate in time. Simulation results using the same numerical code have demonstrated good agreement with experimental measurements.[6,17]

The tests are carried out in a numerical wave channel 48 m in length. Different numbers of points (i.e., $2^{10}$, $2^{11}$, $2^{12}$, and $2^{13}$) are used to discretize the domain to test the effects of the grid size on the surface slope. We found that the maximum surface elevation, $S_{\max} = (-\partial\zeta/\partial \mathrm{x})_{\max}$, obtained with the four discretizations shows a convergent trend and that using $2^{11}$ or more points provides sufficient accuracy, e.g., around 2.5% variation of $S_{\max}$ if using $2^{13}$ instead of $2^{11}$ points. Similarly, a time step of 0.01 s is sufficiently accurate for our purpose. Details regarding this are referred to Tian *et al.*[22]

In the numerical simulations, initial conditions are generated with surface elevations of five non-breaking, focusing wave groups and linear wave theory. Characteristics of the five non-breaking wave groups and the surface elevation measurements are discussed in detail in Tian *et al.*[6] The overall amplitude of the initial surface elevations are then systematically increased by multiplying by a gain factor, i.e., similar to increasing the gain of the input signal to the wavemaker in the experiments, so that the numerical simulations fail when the gain factor is sufficiently large. The maximum surface slope, $S_{\max}$, within a few time steps prior to the numerical failure is recorded and presented in Figure 17. As shown, $S_{\max}$ increases as the gain factor increases for a given wave group. For the cases with no numerical problems, $S_{\max}$ can reach 1.02; for the cases where the simulation fails, $S_{\max}$ is greater than 0.95 (solid symbols). Therefore, to be conservative, we choose a critical value, $S_C = 0.95$, above which numerical singularities may soon occur, corresponding to physical wave breaking.

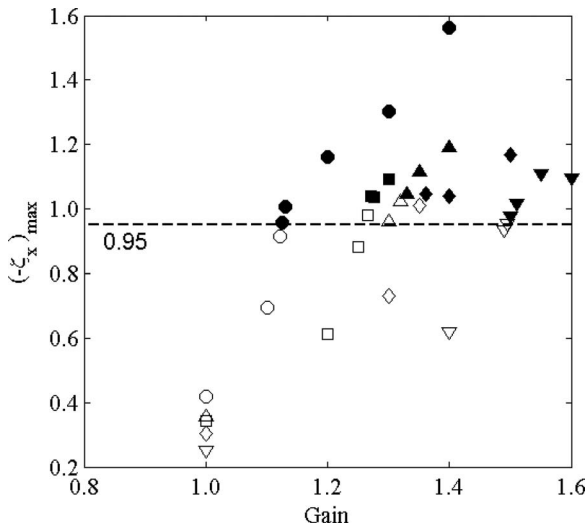


FIG. 17. Determination of a critical local surface slope for wave breaking prediction in the numerical simulations. In the numerical simulations, initial conditions are generated with linear wave theory and surface elevations of five non-breaking, focusing wave groups (i.e., W1G1, W2G1, W3G1, W4G1, and W5G1). Characteristics of these five non-breaking wave groups and surface elevation measurements are discussed in detail in Tian *et al.*[6,22] Solid symbols: wave breaking cases (numerical failure); open symbols: non-breaking groups. Circles for W1G1; diamonds for W2G1; squares for W3G1; triangles for W4G1; and down-pointing triangles for W5G1. The abscissa, Gain, indicates the multiplier of the magnitude of the non-breaking wave groups.


[1] B. J. West, K. A. Brueckner, R. S. Janda, D. M. Milder, and R. L. Milton, "A new numerical method for surface hydrodynamics," J. Geophys. Res. **92**, 11803, doi:10.1029/JC092iC11p11803 (1987).
[2] W. Bateman, C. Swan, and P. Taylor, "On the efficient numerical simulation of directionally spread surface water waves," J. Comput. Phys. **174**, 277 (2001).
[3] A. Goullet and W. Choi, "Nonlinear evolution of irregular surface waves: Comparison of numerical solutions with laboratory experiments for long crested waves," Phys. Fluids **23**, 016601 (2011).
[4] W. Craig and C. Sulem, "Numerical simulation of gravity waves," J. Comput. Phys. **108**, 73 (1993).
[5] W. Choi, "Nonlinear evolution equations for two-dimensional surface waves in a fluid of finite depth," J. Fluid Mech. **295**, 381 (1995).
[6] Z. Tian, M. Perlin, and W. Choi, "Energy dissipation in two-dimensional unsteady plunging breakers and an eddy viscosity model," J. Fluid Mech. **655**, 217 (2010).
[7] D. A. Drazen, W. K. Melville, and L. Lenain, "Inertial scaling of dissipation in unsteady breaking waves," J. Fluid Mech. **611**, 307 (2008).
[8] Z. Tian, M. Perlin, and W. Choi, "Frequency spectra evolution of two-dimensional focusing wave groups in finite depth water," J. Fluid Mech. **688**, 169 (2011).
[9] T. B. Benjamin and J. E. Feir, "Disintegration of wave trains on deep water. 1. Theory," J. Fluid Mech. **27**, 417 (1967).
[10] R. J. Rapp and W. K. Melville, "Laboratory measurements of deep-water breaking waves," Philos. Trans. R. Soc. London, Ser. A **331**, 735 (1990).
[11] M. P. Tulin and T. Waseda, "Laboratory observations of wave group evolution, including breaking effects," J. Fluid Mech. **378**, 197 (1999).
[12] F. Ursell, R. G. Dean, and Y. S. Yu, "Forced small-amplitude water waves: a comparison of theory and experiment," J. Fluid Mech. **7**, 33 (1960).
[13] P. Bonmarin, "Geometric properties of deep-water breaking waves," J. Fluid Mech. **209**, 405 (1989).
[14] J. D. Diorio, X. Liu, and J. H. Duncan, "An experimental investigation of incipient spilling breakers," J. Fluid Mech. **633**, 271 (2009).
[15] J. B. Song and M. L. Banner, "On determining the onset and strength of breaking for deep water waves. Part I: Unforced irrotational wave groups," J. Phys. Oceanogr. **32**, 2541 (2002).
[16] M. L. Banner and W. L. Peirson, "Wave breaking onset and strength for two-dimensional deep-water wave groups," J. Fluid Mech. **585**, 93 (2007).
[17] Z. G. Tian, M. Perlin, and W. Choi, "Evaluation of a deep-water wave breaking criterion," Phys. Fluids **20**, 066604 (2008).
[18] C. H. Wu and H. M. Nepf, "Breaking criteria and energy losses for three-dimensional wave breaking," J. Geophys. Res., [Oceans] **107**(C10), 3177, doi:10.1029/2001JC001077 (2002).
[19] P. Stansell and C. Macfarlane, "Experimental investigation of wave breaking criteria based on wave phase speeds," J. Phys. Oceanogr. **32**, 1269 (2002).
[20] J. H. Duncan, H. B. Qiao, V. Philomin, and A. Wenz, "Gentle spilling breakers: Crest profile evolution," J. Fluid Mech. **379**, 191 (1999).

[21] A. V. Babanin, D. Chalikov, I. R. Young, and I. Savelyev, "Numerical and laboratory investigation of breaking of steep two-dimensional waves in deep water," J. Fluid Mech. **644**, 433 (2010).
[22] Z. Tian, M. Perlin, and W. Choi, "Evolution of nonlinear surface waves under the effects of wave breaking and wind forcing," *The 28th Symposium on Naval Hydrodynamics*, Pasadena, CA, 12–17 September 2010.
[23] K. D. Suh, W. S. Park, and B. S. Park, "Separation of incident and reflected waves in wave-current flumes," Coastal Eng. **43**, 149 (2001).
[24] E. Lamarre and W. K. Melville, "Air entrainment and dissipation in breaking waves," Nature (London) **351**, 469 (1991).